Title

Morphological consequences of ligand exchange in quantum dot - Polymer solar cells

Authors

Hickey, Raymond T
Jedlicka, Erin
Pokuri, Balaji Sesha Sarath
et al.

Publication Date

2018-03-01

DOI

10.1016/j.orgel.2017.12.018

Peer reviewed

Organic Electronics 54 (2018) 119–125

Contents lists available at ScienceDirect

Organic Electronics

journal homepage: www.elsevier.com/locate/orgel

Morphological consequences of ligand exchange in quantum dot - Polymer solar cells

Raymond T. Hickey[a], Erin Jedlicka[b], Balaji Sesha Sarath Pokuri[c], Adam E. Colbert[b], Zaira I. Bedolla-Valdez[d], Baskar Ganapathysubramanian[c], David S. Ginger[b], Adam J. Moulé[d,*]

[a] Department of Materials Science, University of California, Davis, CA, USA
[b] Department of Chemistry, University of Washington, Seattle, WA, USA
[c] Department of Mechanical Engineering, Iowa State University, Ames, IA, USA
[d] Department of Chemical Engineering, University of California, Davis, CA, USA

ARTICLE INFO

Keywords:
Organic photovoltaics
Electron tomography
Quantum dot solar cells
Ligand exchange

ABSTRACT

Mixtures of conjugated polymers and quantum dot nanocrystals present an interesting solution-processable materials system for active layers in optoelectronic devices, including solar cells. We use scanning transmission electron microscopy to investigate the effects of exchanging the capping ligand of quantum dots on the three-dimensional morphology of the film. We created 3D reconstructions for blends of poly((4,8-bis(octyloxy)benzo (1,2-b:4,5-b')-dithiophene-2,6-diyl)(2-((dodecyloxy)carbonyl)thieno (3,4-b)-thiophenediyl)) (PTB1) and PbS quantum dots capped with oleic acid (OA), butylamine (BA), OA to 3-mercaptopropionic acid (MPA), and BA to MPA. We use these reconstructed volumes to evaluate differences in exciton dissociation and charge transport as a function of ligand processing. We show that the MPA exchange without an intermediate BA treatment results in severe changes to the film structure and a non-ideal morphology for an effective device. We also show that with a BA exchange, the morphology remains largely unchanged with the additional MPA treatment. This quantitative characterization elucidates previously reported device performance changes caused by ligand exchange and should inform future device fabrication protocols.

1. Introduction

Solution-processed photovoltaic (PV) devices have been extensively studied due to their potential for fabrication using large scale roll-to-roll manufacturing methods that would result in low cost–per–watt emission–free electricity production. Conjugated polymer-fullerene blends called bulk-heterojunctions (BHJs) have been exhaustively studied with the result that several validated efficiency records exceeding 10% power conversion efficiency (PCE) have been published [1–4]. Quantum dots (QDs) present an alternative to fullerenes as electron acceptors in polymer-based PV devices and pose several advantages including tunable band gap [5], increased thermal stability [6,7], reduced carrier recombination [8,9], and the potential for multiple exciton generation [10,11]. Recent work with polymer-QD films has yielded devices with PCE of up to 5.5% [12] and pure QD devices have been fabricated exceeding 10% efficiency [13].

Improvements in PCE of these devices can be achieved through a better understanding of the morphology resulting from processing conditions. It is widely accepted in organic photovoltaic (OPV) device modeling that the performance of a device could be more completely understood if an accurate three-dimensional map of material location could be measured. High angle annular dark field electron tomography (HAADF-ET) provides a means of acquiring this information. HAADF scanning electron microscopy provides image intensity proportional to the atomic number squared of the species being measured, which creates considerable contrast in the case of PbS particles with a conjugated polymer [14]. A series of projection images of a film in a range of ±65–70° with respect to the beam is acquired and used to create 3D reconstructions of the volume via the discrete algebraic reconstruction technique (DART) [15]. The angular range is limited compared to the ideal ±90° case due to the sample geometry being a film; at angles larger than 70° the film absorbs most of the electrons due to increased effective thickness. The limited angle range results in missing information and the so-called "missing wedge artifacts" in the reconstructions, leading to difficulty in quantifying data especially in the direction of the film thickness [16]. DART is an iterative technique that segments the reconstruction volume into distinct phases with known gray values (exploiting knowledge of density) with each iteration, as

* Corresponding author.
E-mail address: amoule@ucdavis.edu (A.J. Moulé).

https://doi.org/10.1016/j.orgel.2017.12.018
Received 21 September 2017; Received in revised form 2 December 2017; Accepted 16 December 2017
Available online 24 December 2017
1566-1199/

opposed to conventional reconstruction techniques which require a manual segmentation after a complete volume has been reconstructed. DART computes more accurate reconstructions from a small angular range or with noisy projection data than alternative methods [15]. Recently, the DART algorithm has been used to quantify the 3D morphology of P3HT: fullerene blends [17,18]. Although domain size information can be obtained from measuring the photoluminescence quenching of donor/acceptor films using photo-induced absorption, this data is a statistical average assuming spherical domains over the entire volume [9]. Tomographic data is of particular use in that it provides a quantitative three dimensional direct space map of the film morphology, providing details of horizontal and vertical material segregation, as well as domain connectivity and detailed charge-transport pathways.

It is necessary to control the relative solubilities of polymers and QDs to generate a solution processed BHJ mixture. Mutual solubility allows for a well-mixed morphology to develop in one deposition step as opposed to lengthy layer by layer processes. For polymer/fullerene BHJs, the device efficiency depends on several processes that occur at different length scales. Efficient charge separation is governed by diffusion of excitons to a donor acceptor interface with exciton diffusion lengths of 5–10 nm [19,20]. After charge separation occurs, the hole and electron must hop to contiguous adjacent sites with a pathway to the anode and cathode [21]. Finally, the total process efficiency is highest when the hole and electron are prevented from recombining, which is best achieved in a bilayer with minimized interface area between donor and acceptor domains [22]. An ideal BHJ layer would have nanoscale phase separation for optimized exciton separation and also straight pathways for charge transport to both electrodes. Since the materials are mixed in solution this optimized BHJ needs to self-assemble during the drying process.

For polymer/QD BHJ devices, the solubility of the QDs is controlled using a capping ligand [5]. In early devices, little attention was placed on the capping ligand with the effect that in some devices the phase separation was too high due to low solubility of the QDs. In other devices, the QD was highly miscible with the polymer, but the capping ligand was a long chain that prevented charge transport between adjacent QDs [23]. For record holding all-QD (no polymer) PV devices, PbS QDs are deposited and undergo ligand exchanges monolayer by monolayer, resulting in a highly uniform film at the cost of labor-intensive fabrication [8,24–26]. In contrast, the single-step film deposition of polymer–QD blend films is more aligned with the requirements of large scale fabrication.

More recently, blends of polymer/QD BHJs were fabricated in two steps. First films with long chain ligands (typically oleic acid (OA)) on the QD are coated to create a well mixed film. Then in a post deposition processing step, the long chain ligand is replaced with a shorter chain ligand to improve the charge hopping between QDs and to maintain high efficiency photogeneration [23,27–30]. This processing step, known as ligand exchange, is depicted in Fig. 1 along with the ligands studied here. Several different short chain ligands have been investigated including butylamine (BA), which is simply shorter [29], ethanedithiol (EDT), which could bind two different QDs [31], and mercaptopropionic acid (MPA) that is shorter and improves inter-particle electronic coupling [32]. These three short chain ligands have notably different polarities with MPA > EDT > BA which could strongly affect miscibility with the non-polar polymer. It has also been reported that ligand exchange in two steps first with BA followed by MPA yields a higher efficiency PV device than a single exchange step using only MPA [31]. In this case, the BA exchange is performed in solution prior to film deposition. It was recently shown that blends of poly((4,8-bis(octyloxy)benzo(1,2-b:4,5-b')-dithiophene-2,6-diyl)(2-((dodecyloxy)carbonyl)thieno (3,4-b)-thiophenediyl)) (PTB1) and PbS QDs show drastically different external quantum efficiencies depending on the ligand exchange processing [31].

The purpose of this article is to quantitatively study the 3D morphology of PTB1/PbS layers with different capping ligands before and after ligand exchange with MPA to determine whether and how much the ligand exchange steps change the BHJ morphology. We focus here on lead sulfide QD's because PbS is a low-band gap material that is composed of earth abundant materials and has been demonstrated to function in solution cast hybrid polymer/QD photovoltaic devices with >5% power conversion efficiency [12]. Furthermore, the high atomic number contrast provided by the QDs provides good imaging conditions for HAADF TEM and tomographic reconstructions [33]. We further validate these electron microscopy methods for blend characterization with a focus on differentiating the morphology of the PTB1:PbS system as a function of processing conditions.

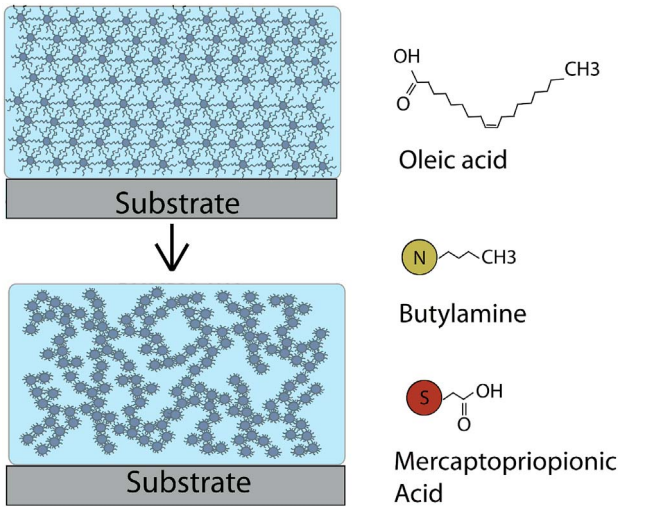

Fig. 1. Schematic of ligand exchange process. As-cast films starting with long OA ligands or shorter BA ligands undergo an in-situ ligand exchange to MPA.

2. Results and discussion

Fig. 2 shows 2D HAADF STEM images comparing 1:9 wt ratio PTB1:PbS films with various capping ligands. HAADF yields Z-contrast

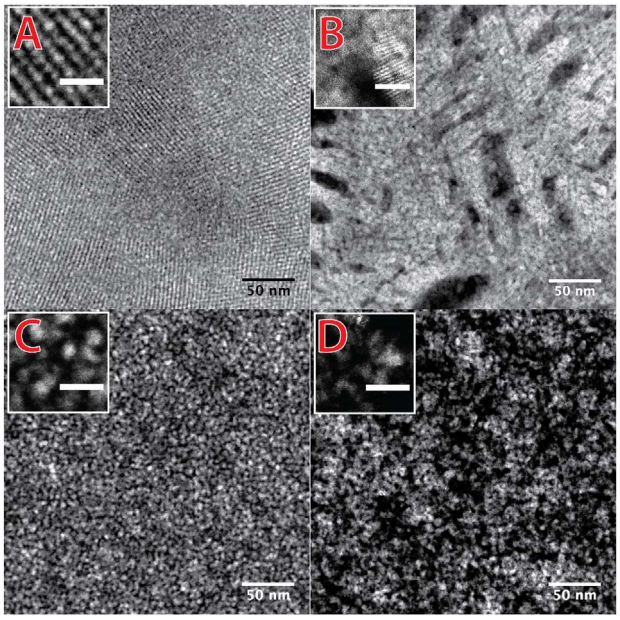

Fig. 2. 2D STEM micrographs showing different morphologies. A - OA as cast. B - OA-MPA treated. C - BA as cast. D - BA-MPA treated. Insets show additional magnification, inset scale bars are 10 nm.

images, wherein the contrast arises from differences in atomic number of the species present. In this case, the light domains correspond to PbS and dark domains are polymer. Z-contrast imaging is only possible by using an inner collection semi-angle that is > 3 times the probe convergence angle [34]. For this study, the inner detection semi-angle was 70 mrad and the convergence semi-angle was 17.1 mrad. The weight ratio is determined from the weight of dry polymer and QDs with OA ligands (Fig. 2A and B) and BA ligands (Fig. 2C and D) before ligand exchange.

Ordered lattice domains of QDs are clearly visible in the as-cast OA sample (Fig. 2A). This order is expected for poorly interacting particles with soft shells [35]. In the OA to MPA exchanged sample (Fig. 2B), large (10–50 nm) dark domains depict defects in the film due to volume shrinkage. The top surface of this film is therefore quite rough. In addition, smaller scale structuring occurs during ligand exchange to yield sheets or wrinkles of QDs separated by organic defects. We also assign this smaller scale structuring to mechanical deformation due to loss of ligand volume upon ligand exchange. For the as cast BA film (Fig. 2C), the individual nanoparticles are still visible and appear to assume a completely random configuration. The ordering seen in Fig. 2A is no longer present for these harder sphere non-interacting nanoparticles. In addition, the film is more dense than the OA cast film but has no large scale defects as seen in Fig. 2B. Finally, the BA to MPA exchanged film (Fig. 2D) has the same dense random structure as the BA cast film but also a hierarchical ordering as seen in the larger dark shadows in the film and clusters of QDs in the inset. There are no large defects in the film as seen in Fig. 2B after a OA to MPA ligand exchange. We can conclude that the solution exchange to a BA ligand before mixing with the polymer and spin coating is useful because it creates a more compact film that does not introduce large scale structural defects upon MPA exchange. Some phase segregation still occurs at the nanoscale but does not introduce structural defects in the already compacted film.

AFM images in Fig. 3 show that the OA samples are rougher both as-cast and post ligand exchange. The well-ordered super-lattice arrays of QDs capped with OA formed during spin coating form lateral domains on the length scale of 100's of nm with clear domain boundaries marked

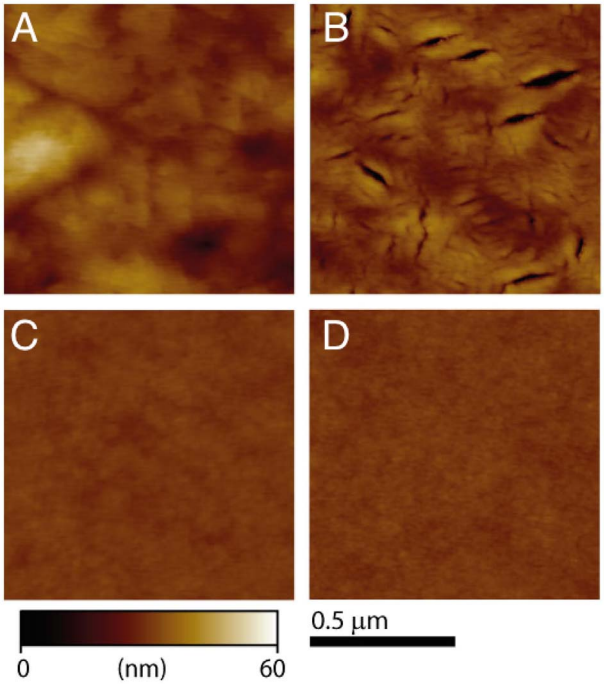

Fig. 3. AFM images of the PbS-PTB1 films. A: OA as cast. B: OA-MPA treated. C: BA as cast. D: BA-MPA treated. The images show the cracking induced by loss of ligands in the MPA exchange on the OA sample, as well as the relative similarity between the BA as cast and BA-MPA films.

Table 1
Structural information.

Sample	Dense QD Volume Fraction (%)	Dense QD Surface Area/Volume Ratio (%)	RMS Surface Roughness (nm)
OA	19.4 ± 2.5	40.2	4.97
OA-MPA	27.7 ± 2.5	25.6	4.22
BA	18.6 ± 2.5	35.1	0.91
BA-MPA	21.1 ± 2.5	37.7	1.02

by height changes. In comparison, the films spin coated with QDs capped by BA ligands are uniform and smooth, which suggests that the amorphous ordering seen in Fig. 2 does not lend itself to domain formation. Table 1 shows RMS surface roughness measurements from the AFM images indicating that the OA samples are 4–5 times rougher than the BA samples. Fig. 3B shows the tearing of the film caused by the OA to MPA exchange. Visual inspection shows that many of the tears are parallel to each other, suggesting that the tears propagate along the planes of the QD superlattice that was formed in coating the OA particles.

In order to investigate this further, we analyzed the tear direction with respect to the orientation of the image and plotted this tear direction. Fig. S1 shows that the orientation of these tears are preferentially at ~60°, suggesting that the QD nanoparticles form in a hexagonal pattern and that when the ligands are exchanged, the volume shrinkage causes the formation of tears along the crystal planes of the QD superlattice. The fact that the tears are oriented over a relatively large area means that the superlattice domains have a significant degree of long-range ordering. Fig. 3D shows a nearly featureless surface with very low surface roughness, which shows that ligand exchange from BA to MPA within the film occurs without significant changes to the morphology. All of the data indicates that there is little reconstruction or mass diffusion of QD particles during ligand exchange.

All of the above data shows what can be learned about the polymer/QD morphology from surface specific or 2D measurements. However, these measurements do not provide quantitative insight into the detailed distribution or vertical composition of these polymer/QD composites. To access this information we used HAADF-ET to measure, and DART to reconstruct, 3D volumes of the sample. The full images are shown in supporting information Fig. S2. These images contain concentration vs position information over a volume of 110 nm × 242 nm × 43 nm with a resolution of 1.1 nm × 1.1 nm × 2.2 nm. To facilitate visualization, Fig. 4 shows a smaller 20 × 20 × 20 nm volume that is representative of the film while also showing the fine nanoscale structure. Fig. 4A shows the OA as cast film, Fig. 4B shows the OA-MPA film, Fig. 4C shows the BA as cast film, and Fig. 4D shows the BA-MPA film. In order to quantify the composition of these reconstructions, we assigned the high-density phase as close-packed PbS particles with just ligands between them, comprising ~20% of the volume. In order for the mass balance of the reconstruction to match the known composition of the deposited film, the remaining 80% of the volume is comprised of a ~5:1 wt ratio of PbS:PTB1 mixture consisting of less densely packed PbS nanoparticles surrounded by polymer. The phases represented here are the solution from the DART algorithm that provided the least amount of error when compared to the original STEM images. We evaluated a number of different phase compositions to determine the accuracy and precision of the reconstructions; this analysis can be found in supporting information Fig. S4.

In general, 3D voxels are not able to capture the ligand shell around individual QDs, but instead show the longer range phase separation between QDs and mixed PTB1/QD phases. The smallest features in each image depict individual QDs at the edge of a QD domain. Comparing the images we can show that the pure PbS domains get larger with ligand exchange of OA to MPA, and remain roughly the same size going from BA to MPA. This observation can be quantified by calculating the reduced surface area (meaning SA between phases but not including the

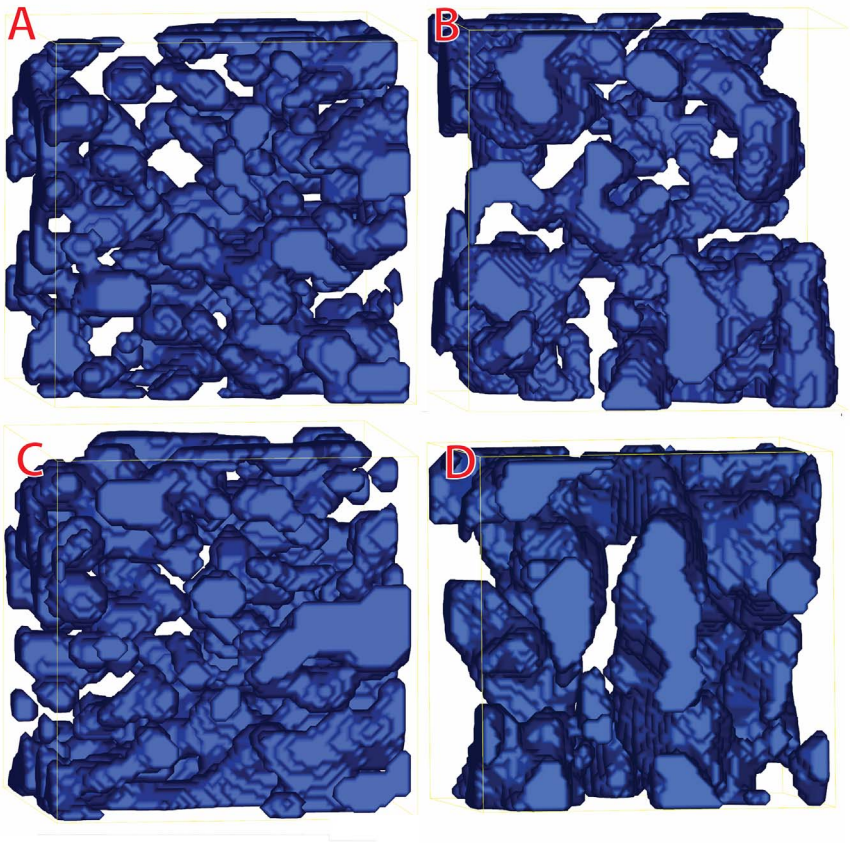

Fig. 4. Three dimensional DART reconstructions of the PbS phase in the films. A - OA as cast. B - OA-MPA treated. C - BA as cast. D - BA-MPA treated. Reconstructed volume is a cube with side length of 20 nm. Negative space represents the PTB1 phase, as well as voids in B.

image interface) of the dense PbS domains and then determining the ratio of surface area:volume fraction of the pure PbS phase before and after ligand exchange, shown in Table 1.

Figs. 2b and 3b both show the formation of large voids in the films that underwent ligand exchange from OA to MPA. These features also exist in the 3D reconstruction of the HAADF-ET data but are not visible in Fig. 4b because only the PbS phase is displayed. The image implies that the remaining volume is only composed of the mixed PbS/PTB1 phase but the void space is also transparent. In order to reconstruct the negative space representing the defects, we reconstructed the OA to MPA exchanged volume using three gray levels, as opposed to the other reconstructions that used two. The combination of the two solid phases from the same volume as Fig. 4b is shown in Fig. S5 with voids being visualized as the negative space. The total void space volume of the OA to MPA exchanged sample is 8.8%. The voids are found throughout the depth of this film, varying in size from the large voids seen in Figs. 2b and 3b down to voids on the same size scale as QD clusters.

As we reported previously [36,37], it is important to have an independent measure of material distribution for validation of the tomographic reconstruction. In this article we provide this independent measurement by comparing the vertical distribution of materials. Fig. 5A shows the effect of ligand exchange on the composition of the film as a function of depth. The OA film has a relatively uniform concentration across its depth. The OA-MPA film appears to have PbS segregation at both electrode interfaces, with a preference towards the bottom (substrate) interface. Since the post-deposition ligand exchange occurs at the top of the film first, and there is significant creation of voids during this process, it is likely that there is PbS enrichment towards the bottom of the film. The BA and BA-MPA films show segregation of the dense QD phase towards the center of the film, possibly a result of poorer miscibility with the polymer and a higher surface energy for ligands to be at the interface.

In order to validate the vertical concentration information from the tomographic reconstructions, we performed glow discharge optical emission spectroscopy (GDOES). GDOES shows qualitative agreement with the vertical concentration information from the tomographic reconstructions, as shown in Fig. 5B, giving us confidence in these results. The OA film has increased density of PbS near the surface in both measurements. The OA-MPA sample shows two peaks of PbS density in both measurements and quantitative agreement on the QD concentration across the whole film thickness. The vertical concentration data from tomography shows an even distribution of PbS QDs in both BA cast samples with some polymer at both top and bottom interfaces. The polymer skin is not visible in the GDOES data but the QD density is mostly flat until the back interface.

The main differences in these measurements are a result of their limitations at the film interfaces. In the DART reconstruction, the sample surface roughness isn't accurately reconstructed, causing some uncertainty in the top and bottom layer of voxels. For GDOES, differences in sputtering rates between the PTB1 and PbS cause the interface to become uneven and results in uncertainty about the atomic ratio, especially at the bottom of the film. This sputtering rate effect can be seen in supplemental Fig. 6 and is especially visible for the OA film, which is likely because the longer carbon containing ligands also etch quickly compared to PbS. Even when taking these limitations into account, the GDOES data provides validation of the reconstructed volumes.

The presence of a “mixed” QD-polymer phase and a “pure” QD phase has important consequences for charge transport within the film. This morphology is qualitatively similar to the PBTTT:fullerene and PTB7:fullerene systems, wherein the device performance is limited by electron transport through the pure fullerene domains [38,39]. In this morphology, excitons within the mixed phase only have to travel a small distance to the nearest QD to be separated into a hole on the polymer and an electron on a QD. In principle, excitons in the polymer could be separated at the interface between mixed phase and the dense

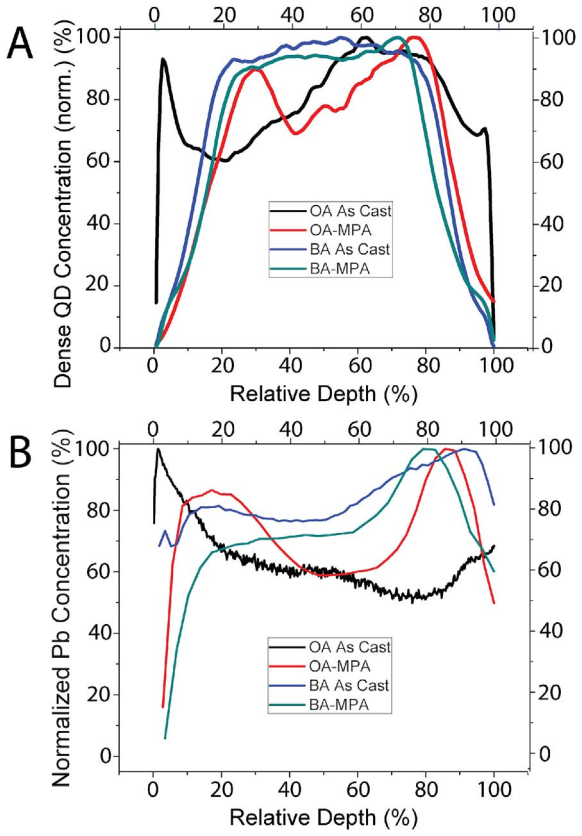

Fig. 5. Film composition as a function of depth; the top surface is 0% depth. **A**- Dense QD phase concentration as a function of depth from the DART reconstructions. **B** - Glow discharge optical emission spectrum showing Pb concentration as a function of depth into the film. The Pb concentration is represented here as the ratio of Pb signal to Pb + C signals. At ~80% depth, the disparity in etch rate causes signal from the substrate to complicate the overall signal. The complete set of signals, including the indium signal from the substrate, can be found in Fig. S6.

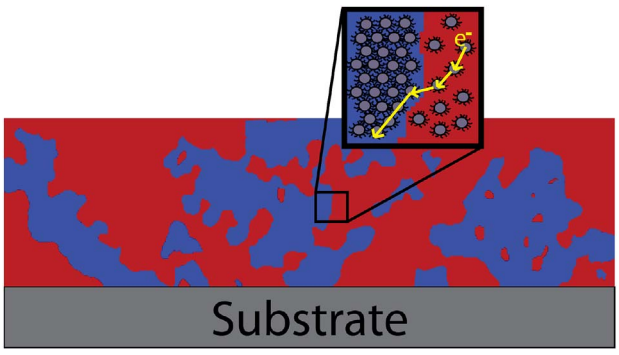

Fig. 6. Illustration showing density differences in reconstructed regions. The dense QD phase (in blue) is purely PbS nanoparticles and the capping ligands, while the lower density phase (in red) is a mixture of QDs and PTB1. The inset shows an example of an exciton from the polymer separating at the interface of a QD, and the possible pathway for subsequent electron transport. (For interpretation of the references to color in this figure legend, the reader is referred to the Web version of this article.)

QD phase, but for the majority of the polymer volume the closest sites for exciton separation are QDs in the mixed phase. Holes are transported to the anode electrode through the well-connected mixed domains. However, electrons created on QDs in the mixed domain must first travel to the dense QD phase via a hopping transport. Since the probability of a successful hop is exponentially dependent on the distance between QDs [40,41], the ~50% of the mixed phase volume that is occupied by ligands and polymer presents a significant transport barrier. Once an electron reaches the dense QD phase, charge transport

Table 2
Electronic information from 3D reconstructions.

Sample	Connectivity of Dense QD Phase to Electrode (%)	Distance 90% of Mixed Phase Lies from Interface with Dense Phase (nm)
OA	89.1	4.5
OA-MPA	97.5	11.5
BA	90.1	9.2
BA-MPA	94.5	9.2

to the electrode should proceed without recombination assuming that the dense phase domains have direct and connected domain structures all the way to the electrode.

Table 2 lists the percentage of dense QD phase domains that are directly connected to the cathode for each morphology. All of the samples show 90% connectivity and the MPA exchanged samples have 95% or greater connectivity. The pathway for electron transport to the electrodes is schematically depicted in Fig. 6. This analysis establishes that poor electron transport through the mixed phase is the likely performance bottleneck for hybrid polymer/QD PV devices. Inefficient transport in the mixed phase results in increased bi-molecular recombination with holes in the polymer. We do not expect that comparison of hole only and electron only conductivity measurements would indicate that electron transport is a bottleneck because the electrons are transported predominantly through the well connected dense QD phase.

To assess the degree to which hopping transport for electrons limits device performance, we measured the distance from each mixed phase voxel to the closest dense QD interface. Fig. 7 shows plot of the nearest distance vs the cumulative % of voxels within this distance. This data shows that the untreated OA capped films have the shortest distance between mixed and dense phases, which could be interpreted as the thinnest mixed phases. 94% of the voxels are within 5 nm of an interface. With PbS particles that have an average diameter of 2.5 nm, 2–3 electron hops are necessary to reach a dense phase from 94% of the entire mixed phase volume. The distribution of distances is nearly identical for the BA and BA-MPA samples with ~80% of the mixed phase volume within 5 nm of a phase interface. The BA samples have a nearly identical morphology in this respect, with more separation than the OA sample due to the more disordered and thicker QD domains. The voids in the OA-MPA film act as barriers that limit pathways to a mixed/QD phase interface. Only ~65% of the mixed phase is within 5 nm of a phase interface.

As reported previously [31], an OA-MPA device has a much lower

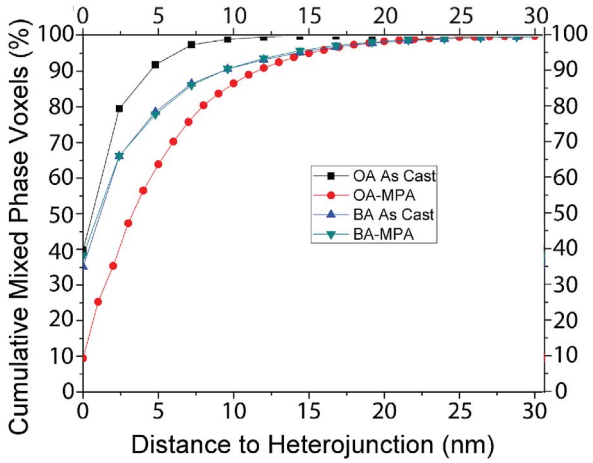

Fig. 7. Percentage of polymer voxels that are within a certain distance of the heterojunction for the different ligand exchanges. The distance that 90% of mixed phase voxels lie within from the interface is shown in Table 2.

short-circuit current density (J_{SC}), and higher open-circuit voltage (V_{OC}), than a BA-MPA device. This result can be explained by the morphological features in the DART reconstructions. The larger volume fraction and lower surface area/volume ratio of dense QD phase in the OA-MPA sample result in the larger V_{OC}, consistent with recent device modeling [42,43]. The larger distance to the donor/acceptor interface (Table 2) for the OA-MPA means the electrons must travel farther to reach the dense QD phase, increasing the likelihood of recombination and thus limiting the J_{SC} in this device [44].

3. Conclusions

In summary we studied the morphology of the polymer PTB1 and PbS quantum dots, a film mixture that shows promise for solution processed photovoltaic applications. Using reconstructed tomographic images we determined that two separate phases form on the nanoscale in all samples: one composed of pure QD nanoparticles and the other composed of a ~5:1 wt fraction QD to polymer mixture. The volume fraction of the dense QD phase was on average $20 \pm 2.5\%$ for all of the films except the OA to MPA exchanged film, that had a 27 ± 2.5 vol% dense QD phase. The OA to MPA exchanged film also had 8 vol% void space from the volume change upon exchange. In the films with BA to MPA exchange there was no defect formation and aside from some ripening of the dense QD phase little change in morphology. This shows that performing a solution exchange of OA to BA is beneficial to the fabrication process because the in-film exchange of OA to MPA leads to a high defect density while there is little morphological change when exchanging from BA to MPA.

We compared the vertical composition of the tomographic data to a separate measurement of vertical concentration from glow discharge optical emission spectroscopy (GDOES). We found strong qualitative and quantitative agreement between the two measurements, which validates the accuracy of the tomographic reconstruction.

We analyzed the tomographic data to determine how the ligand exchange could affect the morphology of the film and thereby the photovoltaic efficiency of a device. We determined that the OA to MPA exchange would create a much larger hopping distance for electrons in the mixed phase and thus increase the likelihood of charge recombination. By comparison, the BA to MPA exchanged sample had nearly identical hopping distance from the mixed phase to a dense QD phase interface as the as-cast BA film. We show that the morphological information from our 3D reconstructions explains previously reported differences in device performance.

4. Experimental

4.1. PbS quantum dot synthesis

Both the butylamine (BA) and oleic acid (OA) capped PbS quantum dots were prepared using an adapted version of the Hines and Scholes protocol [5]. In a 100 mL three-neck round bottom flask, 900 mg (4.0 mmol) of PbO, 28 g of 1-octadecene (ODE)(technical grade, 90%) and 2.4 g (8.5 mmol) of oleic acid were combined and stirred at 100 °C under vacuum for a minimum of 1 h to dissolve the lead precursor as well as degas and dry the solution. After heating, the solution changed color from yellow to clear indicating the PbO completely dissolved. The temperature of the reaction flask was lowered to 90 °C and returned to nitrogen flow while the sulfur precursor solution was prepared. In a separate three-neck round bottom flask, 8 g of ODE was degassed under vacuum for at least 30 min prior to the addition of 420 µL of hexamethyldisilathiane (HMDS). The sulfur precursor was then immediately injected into the hot lead precursor solution to form the PbS quantum dots.

Successful creation of the PbS quantum dots was evident by the change from a colorless solution to a black solution following the injection of the sulfur precursor. After the injection the heat was turned off allowing the reaction to slowly cool down to room temperature. The product was divided in half prior to being isolated from unreacted precursors via methods previously reported [31]. Following isolation and cleaning of the products, one half of the products were treated with butylamine using a solution-based ligand exchange. To exchange ligands, PbS QDs were dissolved in ~2 mL of butylamine and underwent 30 min of sonication. This process was performed twice to ensure full replacement of the native oleic acid ligands. Finally, both the BA treated PbS QDs and OA capped PbS QDs were dried under nitrogen flow and transferred into a nitrogen glove box. The QDs were dispersed in ~2 mL of anhydrous 1,2-dichlorobenzene and stored in the glove box until use.

4.2. Preparation of PTB1/PbS films

PTB1 polymer solution (10 mg/mL concentration) was prepared in a nitrogen glove box by adding an appropriate amount of anhydrous 1,2-dichlorobenzene to PTB1 polymer (1-Material) and heating the solution to 70 °C while stirring until fully dissolved. The polymer/QD blend solution was prepared to be a 1:9 (w/w) ratio with both the polymer and the PbS solutions filtered using a 0.45 µm PTFE syringe filter prior to blending. The blend solution was heated to 70 °C and stirred for 1 h before filtering and spin coating onto ITO/PEDOT:PSS substrates.

To prepare the ITO/PEDOT:PSS substrates, ITO substrates were cleaned by sonication for 20 min in the each of following solutions: 2% Micro-90 detergent, DI water, acetone, and isopropanol. Following cleaning, the substrates were dried with nitrogen gas and plasma cleaned for 5 min immediately prior to spin coating the PEDOT:PSS layer. Approximately 100 µL of PEDOT:PSS was deposited onto the substrate before spinning for 1 min at 3000 rpm. Immediately after spin coating, substrates were placed on a hot plate at 120 °C for 30 min to anneal the PEDOT:PSS layer.

The blend solution was then spun onto the substrates at 1000 rpm for 90 s. Ligand exchange was performed as previously described using a 10 mmol 3-mercaptopronic acid (MPA) [31]. The MPA solution was made in acetonitrile to ensure no PEDOT:PSS was dissolved during the ligand exchange.

4.3. STEM imaging and reconstruction

The films were exposed to DI water to dissolve the PEDOT:PSS layer and release it from the substrate, and were then collected from the surface of the water on a TEM grid. All STEM images used for the reconstructions were taken with a JEOL 2100F at 200 kV. The beam convergence semi-angle was 17.1 mrad and the inner detection semi-angle was 70 mrad. Tilt series were obtained using dynamic focus via a tomography plugin for DigitalMicrograph (Gatan). Images were taken using a Saxton interval scheme from a minimum range of $+65$ to $-65°$ and a maximum range of $\pm 70°$. The electron dose for each image was ~7 electrons per square Angstrom. Image stack alignment was performed manually using IMOD [45], and 3D reconstructions were created using the ASTRA Tomography Toolbox. The voxel size of the reconstructions is 0.35 nm [46,47]. Final volumes were visualized using IMOD.

4.4. AFM imaging

AFM images were measured using a Veeco Multimode AFM in tapping mode at 1.0 Hz.

4.5. GDOES analysis

GDOES analysis was conducted on samples using a Horiba GD-Profiler-2 with a sampling time of 0.050 s at an applied power of 2.50 W and argon pressure of 4 Pa. The area of analysis was 4 mm diameter circle roughly centered on a 1 cm by 1 cm sample.

4.6. Graph analysis

Morphology traits like connectivity to electrodes and distance of voxels to interfaces have been correlated with device performance. We utilized a fast and efficient approach to extracting morphology traits that consisted of converting the reconstructed morphology into an equivalently colored and weighted graph [48–50]. This was done by considering each voxel as a graph vertex (with the color of the vertex determined by the phase of voxel – black vertex for mixed phase and white vertex for QD). The edges of the graph are just constructed by connecting each vertex (or voxel) to its neighbors. The weight of each edge is the geometric distance between the voxel centers. The interface between the pure QD and mixed phase is identified by edges that connect vertices of different color. Vertices having an interface edge are considered as sites for exciton dissociation. The electrodes are represented as meta-vertices in the graph, which are directly connected to the top-/bottom-layer. Connectivity is calculated as the percentage of voxels that are directly connected to the respective electrode (meta-) vertex. Distance to the closest interface is calculated using Djikstra's algorithm.

Conflicts of interest

There are no conflicts to declare.

Acknowledgements

This research was primarily funded by the U.S. National Science Foundation under award No. 1436273. RTH also thanks the Advanced Solar Technologies Institute for partial funding of his salary. ZIB-V thanks the UCMexus-CONACyT postdoctoral fellowship program for salary support (AFM images).

Appendix A. Supplementary data

Supplementary data related to this article can be found at http://dx.doi.org/10.1016/j.orgel.2017.12.018.

References

[1] J. You, L. Dou, K. Yoshimura, T. Kato, K. Ohya, T. Moriarty, K. Emery, C.-C. Chen, J. Gao, G. Li, Y. Yang, Nat. Commun. 4 (2013) 1446.
[2] J.-D. Chen, C. Cui, Y.-Q. Li, L. Zhou, Q.-D. Ou, C. Li, Y. Li, J.-X. Tang, Adv. Mater. 27 (2015) 1035–1041.
[3] Y. Liu, J. Zhao, Z. Li, C. Mu, W. Ma, H. Hu, K. Jiang, H. Lin, H. Ade, H. Yan, Nat. Commun. 5 (2014) 1.
[4] S. Nam, J. Seo, S. Woo, W.H. Kim, H. Kim, D.D. Bradley, Y. Kim, Nat. Commun. 6 (2015) 1.
[5] M.A. Hines, G.D. Scholes, Adv. Mater. 15 (2003) 1844–1849.
[6] L. Chang, I.E. Jacobs, M.P. Augustine, A.J. Moulé, Org. Electron. 14 (2013) 2431–2443.
[7] L. Chang, H.W. Lademann, J. Bonekamp, K. Meerholz, A.J. Moulé, Adv. Funct. Mater. 21 (2011) 1779–1787.
[8] Z. Ning, D. Zhitomirsky, V. Adinolfi, B. Sutherland, J. Xu, O. Voznyy, P. Maraghechi, X. Lan, S. Hoogland, Y. Ren, Adv. Mater. 25 (2013) 1719–1723.
[9] K.M. Noone, S. Subramaniyan, Q. Zhang, G. Cao, S.A. Jenekhe, D.S. Ginger, J. Phys. Chem. C 115 (2011) 24403–24410.
[10] O.E. Semonin, J.M. Luther, S. Choi, H.-Y. Chen, J. Gao, A.J. Nozik, M.C. Beard, Science 334 (2011) 1530–1533.
[11] W.K. Bae, J. Joo, L.A. Padilha, J. Won, D.C. Lee, Q. Lin, W.-k. Koh, H. Luo, V.I. Klimov, J.M. Pietryga, J. Am. Chem. Soc. 134 (2012) 20160–20168.
[12] Z. Liu, Y. Sun, J. Yuan, H. Wei, X. Huang, L. Han, W. Wang, H. Wang, W. Ma, Adv. Mater. 25 (2013) 5772–5778.
[13] X. Lan, O. Voznyy, F.P. García de Arquer, M. Liu, J. Xu, A.H. Proppe, G. Walters, F. Fan, H. Tan, M. Liu, Nano Lett. 16 (2016) 4630–4634.
[14] P. Midgley, M. Weyland, Ultramicroscopy 96 (2003) 413–431.
[15] K.J. Batenburg, J. Sijbers, IEEE Trans. Image Process. 20 (2011) 2542–2553.
[16] Z. Saghi, P. Midgley, Annu. Rev. Mater. Res. 42 (2012) 59–79.
[17] J.D. Roehling, K.J. Batenburg, F.B. Swain, A.J. Moulé, I. Arslan, Adv. Funct. Mater. 23 (2013) 2115–2122.
[18] O. Wodo, J.D. Roehling, A.J. Moule, B. Ganapathysubramanian, Energy Environ. Sci. 6 (2013) 3060–3070.
[19] L.A. Pettersson, L.S. Roman, O. Inganäs, J. Appl. Phys. 86 (1999) 487–496.
[20] D.E. Markov, E. Amsterdam, P.W.M. Blom, A.B. Sieval, J.C. Hummelen, J. Phys. Chem. A 109 (2005) 5266–5274.
[21] P. Peumans, A. Yakimov, S.R. Forrest, J. Appl. Phys. 93 (2003) 3693–3723.
[22] S.R. Forrest, MRS Bull. 30 (2005) 28–32.
[23] A.J. Moule, L. Chang, C. Thambidurai, R. Vidu, P. Stroeve, J. Mater. Chem. 22 (2012) 2351–2368.
[24] A.H. Ip, S.M. Thon, S. Hoogland, O. Voznyy, D. Zhitomirsky, R. Debnath, L. Levina, L.R. Rollny, G.H. Carey, A. Fischer, K.W. Kemp, I.J. Kramer, Z. Ning, A.J. Labelle, K.W. Chou, A. Amassian, E.H. Sargent, Nat. Nanotechnol. 7 (2012) 577–582.
[25] E.H. Sargent, Nat. Photon. 6 (2012) 133–135.
[26] J. Tang, K.W. Kemp, S. Hoogland, K.S. Jeong, H. Liu, L. Levina, M. Furukawa, X. Wang, R. Debnath, D. Cha, K.W. Chou, A. Fischer, A. Amassian, J.B. Asbury, E.H. Sargent, Nat. Mater. 10 (2011) 765–771.
[27] A.M. Munro, I. Jen-La Plante, M.S. Ng, D.S. Ginger, J. Phys. Chem. C 111 (2007) 6220–6227.
[28] A.M. Munro, D.S. Ginger, Nano Lett. 8 (2008) 2585–2590.
[29] A.M. Munro, J.A. Bardecker, M.S. Liu, Y.-J. Cheng, Y.-H. Niu, I. Jen-La Plante, A.K.-Y. Jen, D.S. Ginger, Microchim. Acta 160 (2008) 345–350.
[30] Y. Chen, K. Munechika, I. Jen-La Plante, A.M. Munro, S.E. Skrabalak, Y. Xia, D.S. Ginger, Appl. Phys. Lett. 93 (2008) 053106.
[31] A.E. Colbert, W. Wu, E.M. Janke, F. Ma, D.S. Ginger, J. Phys. Chem. C 119 (2015) 24733–24739.
[32] H. Lu, J. Joy, R.L. Gaspar, S.E. Bradforth, R.L. Brutchey, Chem. Mater. 28 (2016) 1897–1906.
[33] J.C. Hindson, Z. Saghi, J.-C. Hernandez-Garrido, P.A. Midgley, N.C. Greenham, Nano Lett. 11 (2011) 904–909.
[34] P. Hartel, H. Rose, C. Dinges, Ultramicroscopy 63 (1996) 93–114.
[35] Z. Wang, C. Schliehe, K. Bian, D. Dale, W.A. Bassett, T. Hanrath, C. Klinke, H. Weller, Nano Lett. 13 (2013) 1303–1311.
[36] J.D. Roehling, C.W. Rochester, H.W. Ro, P. Wang, J. Majewski, K.J. Batenburg, I. Arslan, D.M. Delongchamp, A.J. Moule, J. Polym. Sci. B Polym. Phys. 52 (2014) 1291–1300.
[37] J.D. Roehling, D. Baran, J. Sit, T. Kassar, T. Ameri, T. Unruh, C.J. Brabec, A.J. Moule, Sci. Rep. 6 (2016) 1.
[38] A.C. Mayer, M.F. Toney, S.R. Scully, J. Rivnay, C.J. Brabec, M. Scharber, M. Koppe, M. Heeney, I. McCulloch, M.D. McGehee, Adv. Funct. Mater. 19 (2009) 1173–1179.
[39] S. Foster, F. Deledalle, A. Mitani, T. Kimura, K.-B. Kim, T. Okachi, T. Kirchartz, J. Oguma, K. Miyake, J.R. Durrant, et al., Adv. Eng. Mater. 4 (2014) 1.
[40] K. Szendrei, W. Gomulya, M. Yarema, W. Heiss, M. Loi, Appl. Phys. Lett. 97 (2010) 203501.
[41] P.R. Brown, D. Kim, R.R. Lunt, N. Zhao, M.G. Bawendi, J.C. Grossman, V. Bulović, ACS Nano 8 (2014) 5863–5872.
[42] T. Zhang, E. Birgersson, J. Luther, Appl. Phys. Express 8 (2015) 024301.
[43] B. Ray, M.S. Lundstrom, M.A. Alam, Appl. Phys. Lett. 100 (2012) 013307.
[44] S.R. Cowan, A. Roy, A.J. Heeger, Phys. Rev. B 82 (2010) 245207.
[45] J.R. Kremer, D.N. Mastronarde, J.R. McIntosh, J. Struct. Biol. 116 (1996) 71–76.
[46] W. van Aarle, W.J. Palenstijn, J. De Beenhouwer, T. Altantzis, S. Bals, K.J. Batenburg, J. Sijbers, Ultramicroscopy 157 (2015) 35–47.
[47] W.J. Palenstijn, K.J. Batenburg, J. Sijbers, J. Struct. Biol. 176 (2011) 250–253.
[48] O. Wodo, S. Tirthapura, S. Chaudhary, B. Ganapathysubramanian, J. Appl. Phys. 112d (2012) 064316.
[49] O. Wodo, S. Tirthapura, S. Chaudhary, B. Ganapathysubramanian, Org. Electron. 13 (2012) 1105–1113.
[50] O. Wodo, J.D. Roehling, A.J. Moule, B. Ganapathysubramian, Energy Environ. Sci. 6 (2013) 3060–3070.